STELLAR ATMOSPHERES. II: THE ANALYSIS OF ABSORPTION LINES

6.1 Introduction

Much of our knowledge of the physical conditions of astrophysical systems relies on spectroscopic observations. The absorption lines formed in the atmospheres of stars contain a wealth of information, on the temperature, gravity, rotational velocity and chemical composition of the star. The last one in particular is of great interest as it reflects (for stars on the main sequence at least) the integrated yields of nucleosynthesis by previous generations of stars. For example, if we can decipher the clues encrypted in the chemical composition of different stellar populations of the Milky Way, we can begin to reconstruct the past history of star formation of our Galaxy (see Figure 6.1).

Another example is offered by the most metal-poor stars known, with metallicities of only 10^{-4} to 10^{-5} of solar metallicity or, in the shorthand commonly used by astronomers, with [Fe/H] $= -4$ to -5. Thus, $[\mathrm{Fe/H}]_{\mathrm{star}} = \log(\mathrm{Fe/H})_{\mathrm{star}} - \log(\mathrm{Fe/H})_{\odot}$. The relative proportions of different elements of the periodic table in the atmospheres of these stars can be very different from their proportions today, as measured in the Sun or in the gas from which stars have recently formed, such as the Orion nebula. Possibly these most metal-poor stars have been enriched by only one previous generation of stars which themselves presumably formed out of pristine gas. Thus, the chemical composition of the most metal-poor stars known is one of the means at our disposal to shed light on the nature of the 'First Stars', sometimes referred to as Population III stars.

A further example is provided by the relative element ratios in the atmospheres of stars that have evolved off the main sequence. In some cases, material deep in the stellar core is 'dredged up' to the surface. The composition of this gas can be quite different from that of the interstellar cloud from which the star originally formed, as a result of the nuclear reactions which have powered the star over the course of its lifetime. Measurements

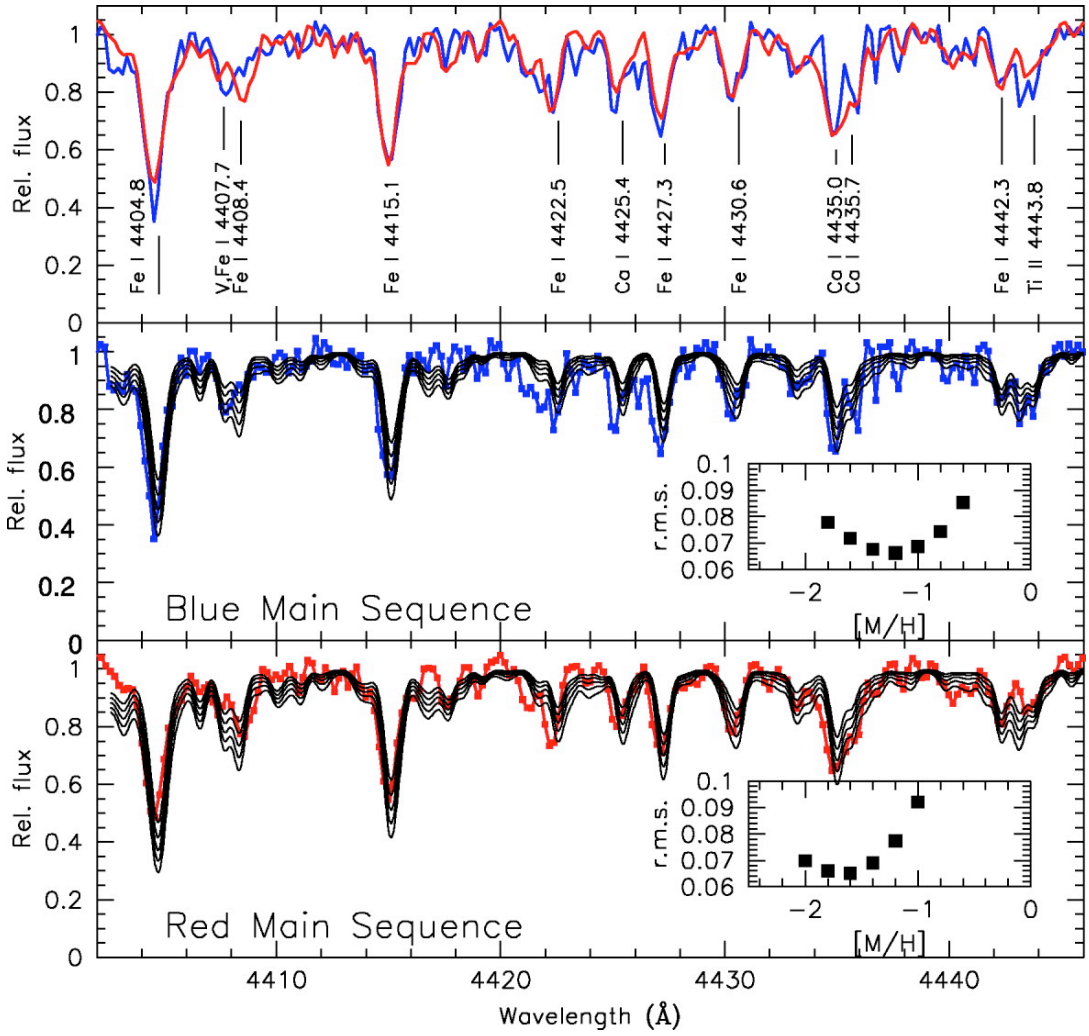

Figure 6.1: The globular cluster ω Centauri (at a distance of 5 kpc in the Galactic halo, with a mass of $10^7 M_\odot$) is unique among Galactic globular clusters in showing two distinct populations of stars, a bluer population and a redder one, with quite distinct main sequences in the colour-magnitude diagram. The origin of these two populations is still unclear. This figure compares a small portion of the average spectrum of 17 blue and 17 red stars, recorded at high resolution with the ESO Very Large Telescope. The top panel shows that there are clear differences in most spectral lines between the two spectra. The middle and bottom panels compare the observed spectra with those produced by model atmospheres with different metallicities [M/H], where M is a 'metal' (Fe, Co, Ti) and $[\mathrm{M/H}]_{\omega\,\mathrm{Cen}} = \log(\mathrm{M/H})_{\omega\,\mathrm{Cen}} - \log(\mathrm{M/H})_\odot$, as indicated. The surprising result is that the blue population is less metal-poor than the red population ($[\mathrm{M/H}] = -1.2$ compared to $[\mathrm{M/H}] \simeq -1.6$), adding to the puzzle that is ω Cen.

of element ratios in the atmospheres of these evolved stars give us the means to check empirically the validity of our ideas as to which nuclear reactions are dominant in stars of different masses.

In order to extract such information from the analysis of stellar spectra, we need to understand how absorption lines are formed in stellar atmospheres.

6.2 Line Equivalent Width

We have already encountered the optical depth τ_λ in the preceding lecture, where we saw that a light beam emerges from the stellar surface with an intensity:

$$I_\lambda = I_{\lambda,0}\, e^{-\tau_\lambda} \tag{6.1}$$

where $I_{\lambda,0}$ is the intensity at its starting point within the star's interior. We also saw that we can write the optical depth in terms of the opacity and the distance travelled

$$\tau_\lambda = \int_0^s \kappa_\lambda \rho \, ds \;\; = \;\; \int_0^s n \, \sigma_\lambda \, ds \, . \tag{6.2}$$

In this lecture we shall use the second equality, where n is the volume density of particles (atoms and ions) and σ_λ is the cross-section for the interaction which, in the case of discrete absorption lines, corresponds to bound-bound transitions, that is electronic transitions between different energy levels.

We define the equivalent width W_λ of an absorption line as the width, in wavelength units, of a rectangular strip of spectrum having the same area

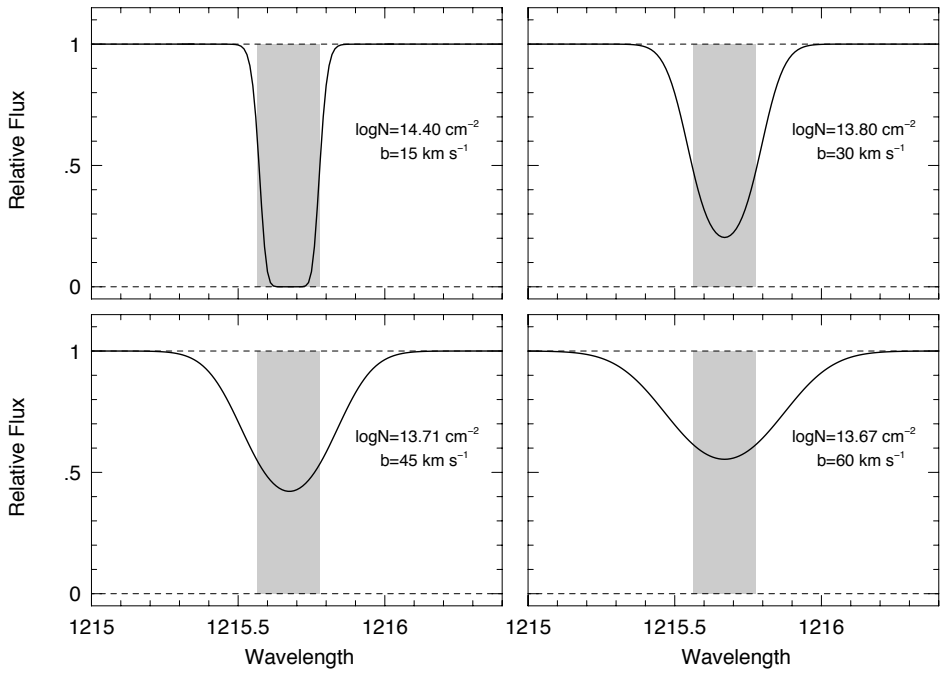

Figure 6.2: Four absorption lines with the same equivalent width (shaded grey area) but different widths, as measured by the value of b (km s^{-1}). N (cm^{-2}) is column density, defined as the number of absorbers in a column of unit cross-sectional area. Figure courtesy of Chris Churchill.

as the absorption line:

$$W_\lambda = \int_0^\infty \frac{I_{\lambda,0} - I_\lambda}{I_{\lambda,0}}\, d\lambda \;=\; \int_0^\infty \left(1 - e^{-\tau_\lambda}\right)\, d\lambda \tag{6.3}$$

The equivalent width is a convenient measure of the strength of an absorption line. Its value lies in the fact that historically the resolution of spectrographs was too coarse to resolve the intrinsic profiles of the absorption lines. What all instrument record is the *convolution* of the intrinsic line shape with the instrumental broadening function; if the latter is broader than the intrinsic width of the absorption line recorded, much of the information encoded in the line profile itself is lost. However, the equivalent width is invariant to the convolution, and is thus a conserved quantity (modulo complications introduced by limited signal-to-noise ratio of the spectra). Some stellar parameters of interest can be deduced from measurements of the line equivalent widths, particularly the relative fractions of atoms and ions in different excitation and ionisation stages and the relative abundances of different elements.

6.3 Line Broadening Processes

The cross-section for absorption, σ_λ, in eq. 6.2 can be written as:

$$\sigma_\lambda = \sigma_0 \cdot \Phi_\lambda \tag{6.4}$$

where σ_0 includes the atomic parameters of the transition

$$\sigma_0 = \frac{\lambda^4}{8\pi c}\, \frac{g_u}{g_l}\, a_{ul} \tag{6.5}$$

where g_u and g_l are the statistical weights of the upper and lower electronic energy levels, a_{ul} is the transition probability and the other symbols have their usual meaning.

Φ_λ is the broadening function, defined so that if an absorption does take place in the line, $\Phi_\lambda d\lambda$ is the probability that the wavelength of the absorbed photon lies between λ and $\lambda + d\lambda$. Thus:

$$\int_0^{+\infty} \Phi_\lambda\, d\lambda = 1 \tag{6.6}$$

The value of Φ_λ is large near λ_0 (the line centre) and falls off rapidly at longer and shorter wavelengths.

In stellar atmospheres, there are a number of physical processes that broaden the absorption lines. The two main processes are:

1. Natural broadening, due to the uncertainty ΔE in the energy of the upper atomic level k, and
2. Doppler broadening due to the motions of the absorbers.

6.3.1 Natural and Pressure Broadening

Considering natural broadening first, we have (for an atom at rest):

$$\phi_\lambda(v=0) = \frac{1}{\pi} \frac{\delta_k}{\delta_k^2 + (\lambda - \lambda_0)^2} \tag{6.7}$$

where δ_k is the radiation damping constant in wavelength units:

$$\delta_k = \frac{\lambda^2}{4\pi c} \sum_{E_r < E_k} a_{kr} \tag{6.8}$$

Thus, the radiation damping constant is inversely proportional to the lifetime of the upper level k, which is related to an intrinsic 'width' of the energy level according to Heisenberg uncertainty principle:

$$\Delta E \approx \frac{\hbar}{\Delta t} \tag{6.9}$$

A line profile given solely by the natural broadening function in eq. 6.7 is sometimes referred to as a damping (or Lorentz) profile because its inverse square functional form is characteristic of the spectrum of radiation emitted by an electric charge undergoing damped simple harmonic motion.

In the dense atmospheres of stars, the electronic energy levels can be perturbed by collisions with neutral atoms and by close encounters with the electric field of an ion. Both processes are often referred to as pressure broadening. The full calculation of pressure broadening effects is a complex matter. For our purposes, let us consider the case where the time

interval between collisions is small compared to the lifetime of the energy level. Collisional de-excitation of the electron will then shorten the lifetime of the atomic level; referring back to eq. 6.9, Δt is reduced and ΔE is therefore increased.

Pressure broadening also produces a damping profile and the overall effect is an increase in the damping constant $\delta_k' = \delta_k + \delta_p$, where δ_p is the number of collisionally induced transitions per unit time. We can obtain an approximate estimate of δ_p by considering the average time between collisions:

$$\delta_p = \frac{1}{\Delta t} \approx \frac{v}{\mu} = \sqrt{\frac{2kT}{m}} \cdot n\sigma_c \,, \tag{6.10}$$

where, as we saw earlier, the mean free path is $\mu = 1/n\sigma_c$ (where n is the particle density and σ_c the collisional cross-section), and the most probable speed is $v = \sqrt{2kT/m}$ for a Maxwell-Botzmann distribution.

In cooler stars, where pressure broadening is most important, collisions with neutral hydrogen atoms are the main source of pressure broadening. Note the dependence of δ_p on n. This explains why the absorption lines in giant and supergiant stars (luminosity classes III to Ia in the MK classification scheme) are narrower than in dwarfs (luminosity class V): the extended atmospheres of (super)giants have lower densities than their counterpart main-sequence stars of the same spectral class.

6.3.2 Doppler Broadening

No atoms is at rest. In reality, the absorbing atoms will have a distribution of radial velocities along the line of sight $\Psi(v)$. There can be several contributions to $\Psi(v)$. At the atomic level, the temperature of the gas results in a corresponding Maxwellian distribution of velocities:

$$\Psi(v) = \frac{1}{\sqrt{\pi} b} \exp\left[-\frac{(v - v_0)^2}{b^2}\right] \tag{6.11}$$

where b, sometimes referred to as the Doppler width, is related to the temperature via:

$$b_{\rm th} = \left(\frac{2kT}{m}\right)^{1/2} \tag{6.12}$$

$b = \sqrt{2}\sigma$ where σ here is the one-dimensional rms velocity projected along the line of sight, while the three-dimensional rms velocity is $v_{\rm rms} = \sqrt{3} \times (b/\sqrt{2})$.

In addition to motions at the atomic level, there can be bulk motions resulting, for example, from different parts of the stellar disk having different velocities. Large-scale convective motions within the photosphere, such as those responsible for the granulation seen on the surface of the Sun, are an example of such macroturbulence. Such macroturbulence can often also be approximated by a velocity distribution similar to eq. 6.11, with an equivalent $b_{\rm turb}$. Other types of large-scale motion, such as rotation, cannot; they give characteristically broadened line profiles that have be treated separately.

Finally, in the analysis of stellar spectra a parameter termed 'microturbulence' is also used, generally as a 'fudge' to explain the fact that the lines appear broader than expected on the basis of the temperature derived by other means. Physically, this additional turbulence can be understood if, along any sightline from optical depth $\tau_\lambda = 2/3$ to the surface of the star, the photons encounter regions of different velocity, introducing an additional Doppler broadening. The total Doppler broadening is obtained by adding the different b-values in quadrature:

$$b^2 = b_{\rm th}^2 + b_{\rm turb}^2 + b_{\rm micro}^2 \tag{6.13}$$

Including Doppler broadening into the broadening function, we now have:

$$\Phi_\lambda = \frac{1}{\pi} \int_{-\infty}^{+\infty} \frac{\delta_k'}{\delta_k'^2 + \left[\lambda - \lambda_0 \left(1 + \frac{v}{c}\right)\right]^2} \Psi(v) dv \tag{6.14}$$

Which of these two main sources of broadening is dominant? Generally, the damping constant δ_k' is much smaller than the Doppler constant b (both in wavelength units); for example, for the Hα line of neutral hydrogen in the Sun, $\delta_k/b \sim 0.001$. However, the dependence of these two types of broadening functions on wavelength is not the same: the probability of the absorption taking place due to Doppler broadening falls off with wavelength from the line centre faster (exponentially, see eq. 6.11) than that due to natural broadening, which has an inverse-square dependence (eq. 6.7). Thus, absorption lines tend to have a Doppler core and damping

wings. Absorption near the line centre is due mostly to the motions of the atoms, while far from the line centre it is the fundamental uncertainty ΔE in the energy of the atomic levels that allows the absorption to take place.

6.4 The Curve of Growth

The full expression for the line optical depth at wavelength λ is obtained by combining eqs. 6.2, 6.4, 6.7, and 6.11 to give:

$$\tau_\lambda = N\,\sigma_0\,\phi_\lambda \bigotimes \Psi(v) \tag{6.15}$$

where the convolution of the natural broadening and Doppler broadening functions is as given in eq. 6.14, and N (cm^{-2})

$$N = \int_0^s n\,ds \tag{6.16}$$

is the column density, which measures the number of absorbers in a cylinder of unit cross-section. The expression 6.15 for τ_λ is often referred to as the Voigt function.

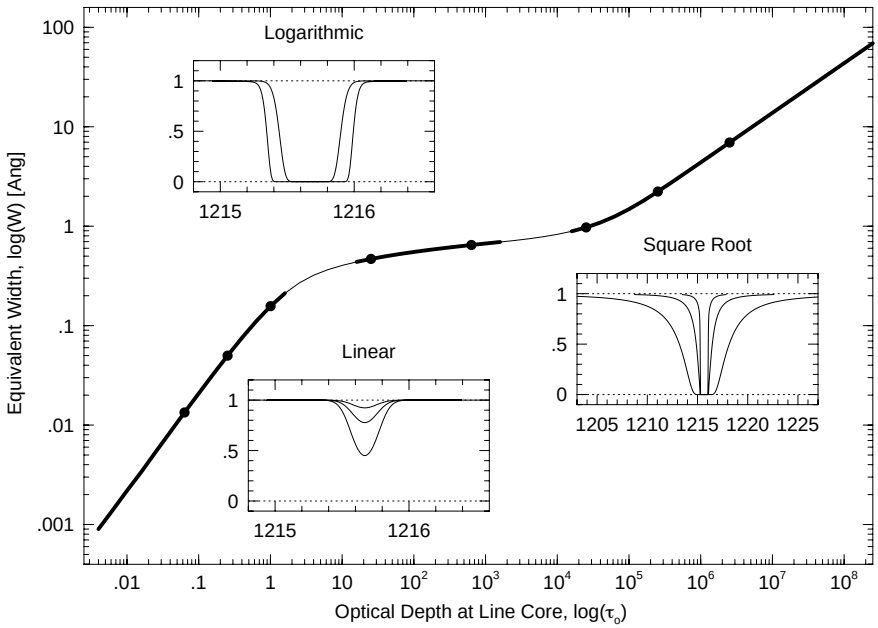

Figure 6.3: Example of a curve of growth. The three regimes discussed in the text, the linear, flat, and damping part of the COG are shown by thicker curves. Corresponding line absorption profiles are shown for each regime and their locations on the COG are marked with filled dots. The wavelength (x-axis) scale in the panel for lines on the damping part of the COG has been expanded relative to the other two panels to illustrate the large extent of damping wings. (Figure courtesy of Chris Churchill).

Integration of 6.3 then gives the sought-after relationship between the equivalent width W_λ of an absorption line and the column density N of absorbing atoms. This relationship, which is illustrated in Fig. 6.3, is known as the Curve of Growth, because it describes how W_λ grows with increasing N.

The precise functional dependence of W_λ on N is sensitive to the optical depth at the line core, τ_0. Qualitatively, as τ_0 increases from $\tau_0 \ll 1$, the residual intensity I_λ in the line core decreases (the line depth increases) until all the photons at the line core are removed from the incoming beam. At this point, the absorption line is considered to be 'saturated'. As τ_0 increases further, very little additional light is removed from the beam until we reach a regime where the optical depth becomes significant at wavelengths far from the line centre, where absorption takes place from the natural broadening of the line. The equivalent width can then grow again, as the line develops characteristic 'damping wings' [where the absorption coefficient falls off as the inverse square of $(\lambda - \lambda_0)$].

Before proceeding, a note of clarification is required here. The above treatment is strictly only valid for a 'foreground screen' of gas illuminated by a background source of light. This situation is an appropriate description of, for example, the interstellar absorption lines seen in the spectra of distant stars and quasars unrelated to the absorbing regions. It is also useful as an approximation to understand the formation of stellar absorption lines. However, recall that at any wavelength we see into a stellar atmosphere from the surface down to $\tau_\lambda = 2/3$. Thus, we see much further into a star in the continuum than in the core of an absorption line. When $\tau_\lambda \gg 1$ in eq. 6.15, and the line profiles intrinsically resemble those shown in the top sub-panel of Figure 6.3, the depth we see into the star approaches zero. But even at the surface of the star, the intensity I_λ is not zero. For LTE, $I_\lambda = B_\lambda \neq 0$, because $T \neq 0$. Thus, in stellar spectra, even strongly saturated absorption lines do not reach down to zero intensity; as a rule, even in the line core, $I_\lambda = I_\lambda(\tau = 2/3)$.

6.4.1 Measuring Column Densities

Returning to Figure 6.3, we can distinguish three portions of the Curve of Growth:

1. **The linear part**, where $\tau_0 < 1$ and $W_\lambda \propto N$. The absorption line is optically thin and W_λ is a sensitive measure of N, irrespectively of the value of the Doppler parameter b.

   Using the approximation $e^{-x} \simeq 1 - x$ when $x \ll 1$, it can be readily seen from eq. 6.3 that on the linear part of the COG:

   $$W_\lambda = \int_0^\infty \tau_\lambda \, d\lambda \;=\; N \, \sigma_0 \int_0^\infty \Phi_\lambda \, d\lambda \;=\; N \, \sigma_0 \qquad (6.17)$$

   since we defined $\int_0^\infty \Phi_\lambda \, d\lambda = 1$ (eq. 6.6).

2. **The flat, or logarithmic, part**, where $10 \lesssim \tau_0 \lesssim 10^3$ and $W_\lambda \propto b\sqrt{\ln(N/b)}$. The absorption line is optically thick and W_λ is *not* a good measure of N, but is sensitive to the Doppler parameter b.

3. **The damping, or square root, part**, where $\tau_0 \gtrsim 10^4$ and $W_\lambda \propto \sqrt{N}$. In this regime, the optical depth in the damping wings provides an accurate estimate of N.

Curves of growth tend to be plotted in a variety of ways. Most commonly, they are a plot of W_λ/λ vs. $Nf\lambda$, where f is the 'oscillator strength' of a transition (available from compilations of atomic data), related to the statistical weights and the transition probability as follows:

$$\lambda \, g_l f_{lk} = \frac{m_e c \, \lambda^3}{8\pi^2 e^2} \cdot g_k a_{kl} \qquad (6.18)$$

In other applications, COGs are plots of W_λ/λ vs. $A\,f\lambda$, where A is the abundance of the element of interest relative to H.

6.4.2 Which Curve of Growth?

The transition between the linear and flat parts of the curve of growth occurs at different values of N depending on the Doppler width b, as can be appreciated from inspection of eq. 6.11 and Figure 6.4. In reality, even for a single absorption line, there is a whole family of COGs depending on the value of the Doppler parameter b, which is generally unknown.

Such ambiguity can be resolved by observing many absorption lines formed in the same layer of the stellar atmosphere. Fe is a good example because of the large number of transitions available between its energy levels. The

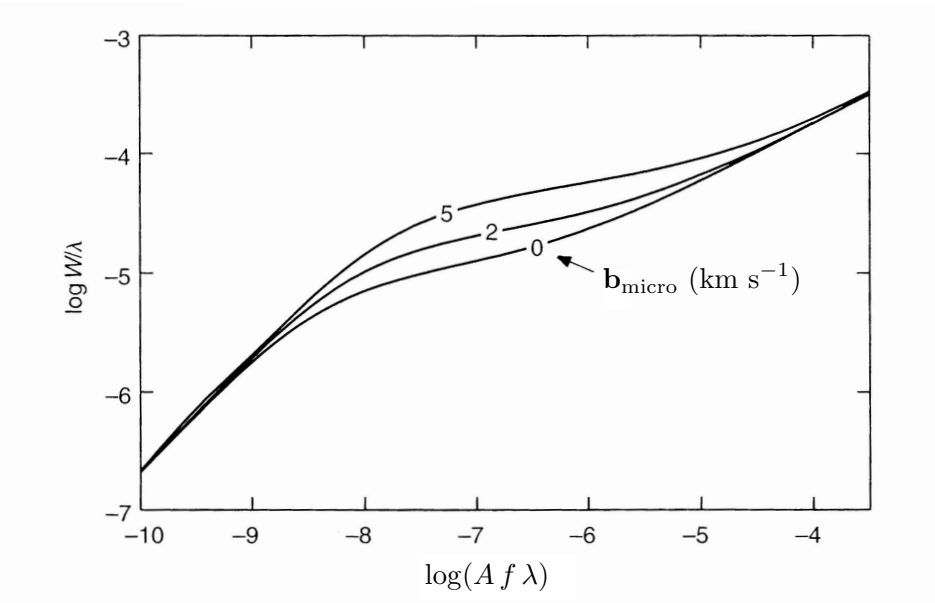

Figure 6.4: Different curves of growth for three values of the microturbulence parameter $b_{\rm micro}$. At greater values of b, the transition between the linear and flat part of the curve of growth occurs at larger values of W_λ and N.

measured values of W_λ/λ can be fitted with a theoretical COG to determine the equivalent Doppler parameter (which is the sum in quadrature of all the individual b-values, see eq. 6.13), as well as the column density of the ion under consideration, as shown in Figure 6.5.

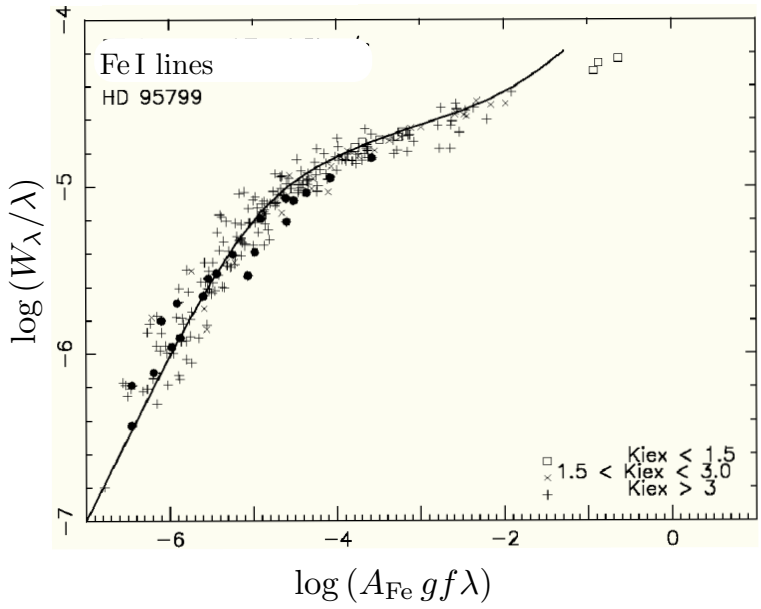

Figure 6.5: Empirical curve of growth for Fe lines in the star HD 95799. Different symbols indicate three ranges of excitation potential for the Fe I lines, while Fe II lines are represented by filled circles. The continuous line is a theoretical curve of growth for $b_{\rm micro} = 1.5\,{\rm km\ s^{-1}}$ and a solar abundance of Fe: $A_{\rm Fe} = 3 \times 10^{-5}$ by number.

There can be limitations to the use of COGs, for example if some of the atomic data relevant to the transitions observed are poorly known. Much of the use of COGs is in differential analysis, where the strengths of a set of absorption lines are compared in different stars, to deduce the relative abundances of the elements of interest (an example was shown in Figure 6.1). Similarly, the ratios of the column densities of two (or more) ionisation stages of the same element in a star can be used to infer the ionisation temperature via the Saha equation (eq. 3.4), if the electron density is known. The ratio of the column densities of two excitation stages of the same ion gives the excitation temperature via the Boltzmann equation (eq. 3.1).

6.5 Measurements of Stellar Parameters from Spectral Lines

Nowadays, the analysis of stellar spectra is generally conducted by comparing the observed spectrum with a suite of theoretical ones computed according to a stellar model atmosphere. In such models, each atmospheric layer is involved in the formation of the line profiles and contributes to the final spectrum. Thanks to advances in computational power, models are being developed with increasing levels of sophistication, taking into consideration the full three-dimensional structure of a star and departures from LTE where necessary. Here we give a few examples.

6.5.1 Metal Lines as Temperature Indicators

The sensitivity of metal lines to temperature can vary widely. Generally speaking, lines of neutral metals are most useful in solar-type stars, while lines of ionised metals are better temperature tracers in hotter stars. Many lines can be analysed at once and the curve of growth can be used as a temperature-measuring device by finding the excitation temperature that minimises the scatter in an empirical curve of growth (see Figure 6.5).

Observational precision can be increased by using the ratio of the central depths of two absorption lines when the stellar spectrum has been recorded at high resolution and signal-to-noise ratio, usually with an echelle spec-

trograph. Ideally one would choose two lines from the same element, so as to eliminate any abundance dependence. However, in practice it is advantageous to use pairs of lines at nearby wavelengths, so as to minimise any errors in the continuum normalisation (i.e. in dividing out the underlying stellar continuum radiation against which the absorption appears to take place). In this case, pairs of lines of similar elements, such as Fe, V and Ti, (elements that are not expected to exhibit differential abundance variations) are used, as shown in Figures 6.6 and 6.7.

There are many such pairs of lines in the spectra of cool stars; an example is reproduced in Figure 6.7. Any given pair of lines is limited in the temperature range over which it is a useful measure of $T_{\rm eff}$. As can be appreciated from the right panel of Figure 6.6, in stars cooler than $T_{\rm eff} \simeq 3900\,{\rm K}$ a different set of lines is needed to measure the temperature.

Application of the line-depth ratio method can yield very high temperature *resolution*, as high as a few K, which is 10–20 times better than the accuracy with which the temperature scale itself can be established.[1] Nevertheless, line-depth ratios are a powerful tool for measuring small temperature differences between stars, or small variations in the temperature of a given star.

[1] A good example of a case where the systematic error overwhelms the random error of a physical measurement.

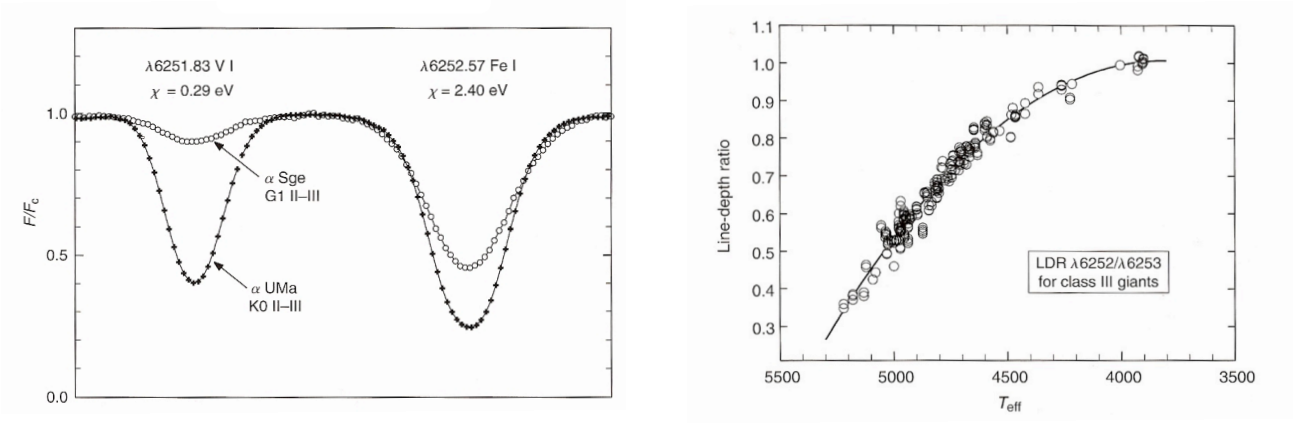

Figure 6.6: *Left:* The ratio of the equivalent widths (or simply the central depths) of two absorption lines originating from atomic levels of different excitation energies, as indicated, can be a sensitive thermometer. *Right:* A typical calibration curve for a line-depth ratio. The slope of the curve reflects the temperature sensitivity of the method. In this case, the line ratio can be used to infer $T_{\rm eff}$ in stars hotter than $\sim 4000\,{\rm K}$. (Figures reproduced from Gray, D.F., Stellar Photospheres, CUP).

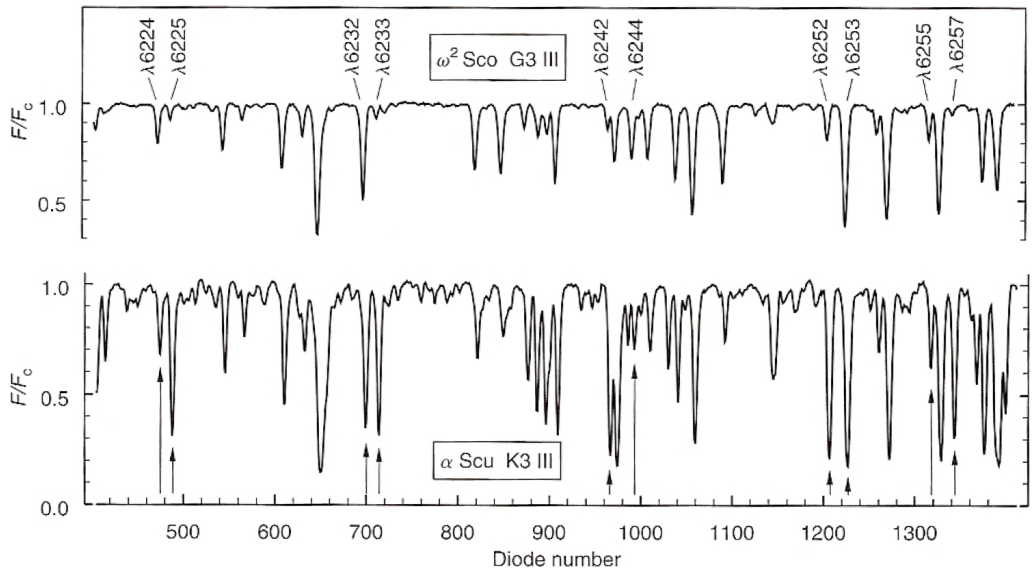

Figure 6.7: Spectral lines having different sensitivity to temperature such as those marked, have been selected in close pairs to avoid continuum setting errors. In these stars, absorption lines of V I vary more strongly than the nearby Fe I lines. (Figure reproduced from Gray, D.F., Stellar Photospheres, CUP).

6.5.2 Spectral Lines as Pressure Indicators

Stars above the main sequence in the HR diagram have higher luminosity and lower photospheric pressure than stars on the main sequence, as a result of their expansion (see Lecture 13). Indeed, pressure effects are often referred to as luminosity effects. Generally speaking, spectroscopic pressure effects are more subtle than temperature effects. On the other hand, while values of $T_{\rm eff}$ span about one order of magnitude between the coolest and the hottest stars, pressure ranges by five orders of magnitude from dwarfs to supergiants. This renders even relatively subtle pressure effects measurable in stellar spectra.

As explained in Section 6.3.1, pressure adds to the natural damping constant to give characteristic broad wings to the absorption lines. From the measurement of these wings, as we shall see in a moment, astronomers deduce the value of *surface gravity*, or $\log g$, where g is the gravitational acceleration (in cm s^{-2}) which would be experienced by a hypothetical test particle of negligible mass at the star's surface. Thus, $\log g = 3$ at the surface of the Earth. Main sequence stars have $\log g \simeq 4.5$, with only a modest dependence on stellar mass. On the other hand, in supergiants $\log g$ varies by three orders of magnitude, from $\log g \simeq 3.5$ in O5 I stars to

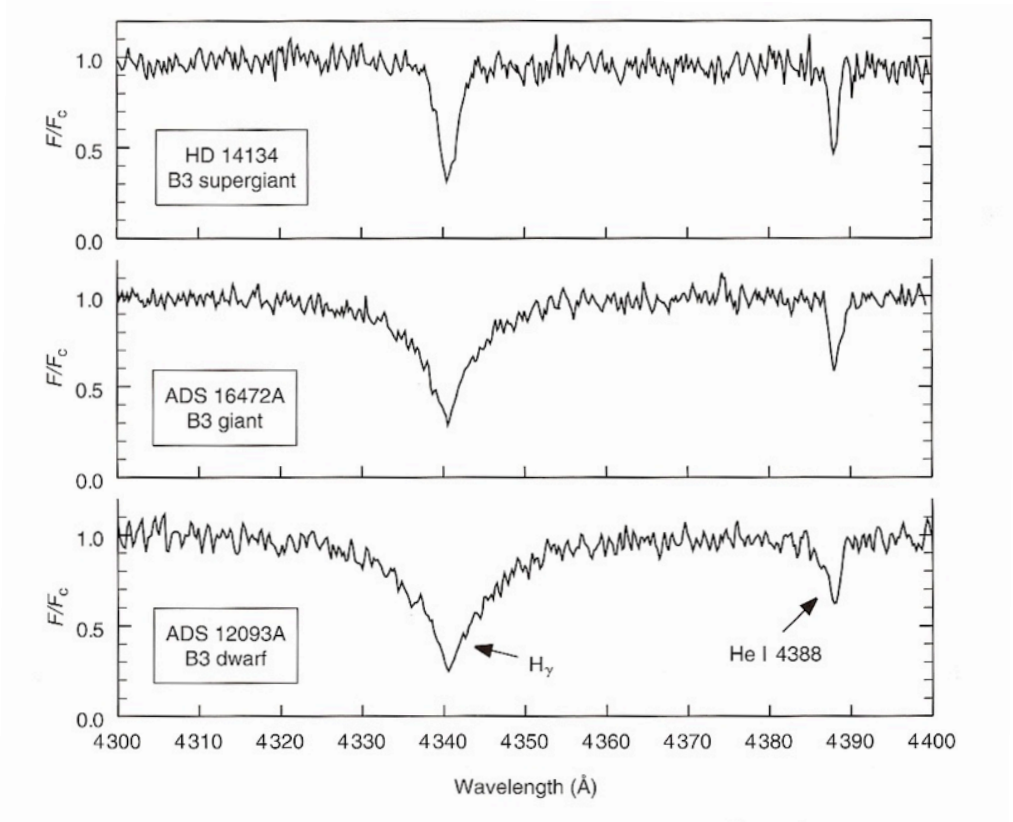

Figure 6.8: Pressure variations in the profile of the Hγ line in B3 stars of different luminosity classes. The effect arises because of the pressure dependence of the linear Stark effect, the broadening of the $n = 2$ and $n = 5$ energy levels of neutral hydrogen due to presence of an external electric field provided by nearby ions. (Figure reproduced from Gray, D.F., Stellar Photospheres, CUP).

$\log g \simeq 0$ in M2 I red supergiants.

Pressure sensitivity in the hydrogen lines of the Balmer series is one of the classical luminosity indicators in early-type stars (see Figure 6.8). Model profiles are shown in Figure 6.9. The gravity dependence rapidly diminishes

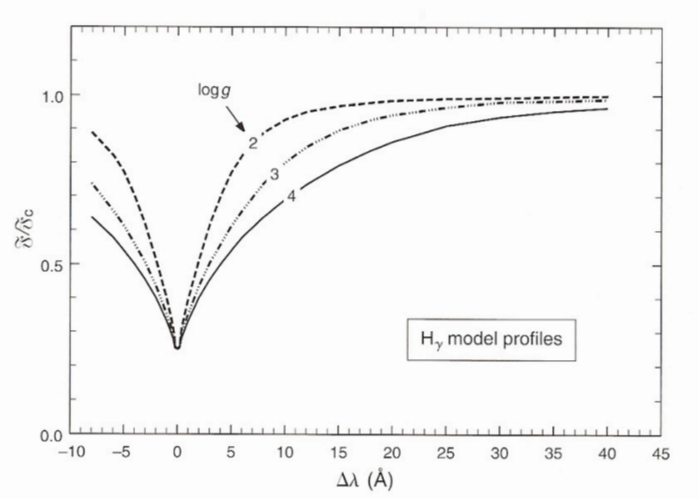

Figure 6.9: Model profiles of the Hγ line of the Balmer series for different values of surface gravity, as indicated. (Figure reproduced from Gray, D.F., Stellar Photospheres, CUP).

with temperature below $T_{\rm eff} \simeq 10\,000\,{\rm K}$.

The Balmer lines can be so strong in stars that their equivalent widths can be determined (approximately) from photometric, rather than spectroscopic, measurements. That is, one compares stellar magnitudes measured through two filters of different bandpasses, both centred on the same Balmer line. The most widely used such index is the Hβ index, which measures the magnitude difference between two filters, each centred at the wavelength of the Hβ line, with half-width bandpasses of 29 Å and 129 Å respectively. The Hβ index is the gravity discriminant in the *uvby* β Strömgren photometric system.

Some strong metal lines also show pressure-broadened wings in the spectra of cooler stars; an example is reproduced in the left panel of Figure 6.10. Since pressure diagnostics are always temperature sensitive, it is often useful to make a simultaneous solution for $T_{\rm eff}$ and $\log g$. This can be achieved if we have two lines that have different responses to the two variables, as in the example shown in the right panel of Figure 6.10. Each curve in this gravity-temperature diagram is computed for a fixed Fe abundance, while varying $\log g$ at a given $T_{\rm eff}$ (or vice versa) to recover the observed equivalent width. The crossing point is then the solution, i.e. the correct

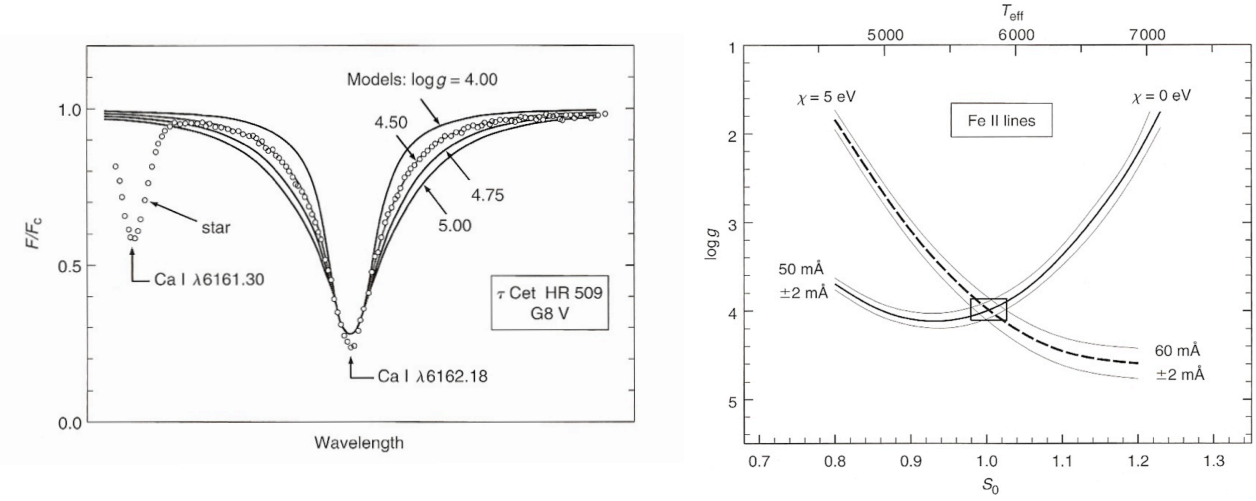

Figure 6.10: *Left*: Fitting theoretical line profiles to the Ca I λ6162 line recorded in the spectrum of the G8 V star τ Ceti gives a measure of the surface gravity: $\log g = 4.50$ *Right:* Gravity–Temperature diagram for the equivalent widths of two Fe II absorption lines of different excitation potential, as indicated. Measurement errors are shown by lighter lines. The solution is localised to the small rectangle where the lines cross. (Figures reproduced from Gray, D.F., Stellar Photospheres, CUP).

effective temperature and surface gravity. The uncertainties in the two parameters can be estimated by mapping the errors ΔW_λ into ranges $\Delta T_{\rm eff}$ and $\Delta \log g$, as shown by the rectangle in the Figure.

A number of diagnostics can be placed on the same $\log g$–$T_{\rm eff}$ diagram and, in theory, all loci should intersect at the same point within the errors ΔW_λ. The real case differs from the ideal case because of inadequate model stellar atmospheres, incomplete understanding of line formation, systematic errors in the data, and other second-order effects.

6.5.3 Abundance Determinations from Metal Absorption Lines

Once the effective temperature and gravity of a star have been determined by rigorous analysis of absorption lines that are sensitive to these two

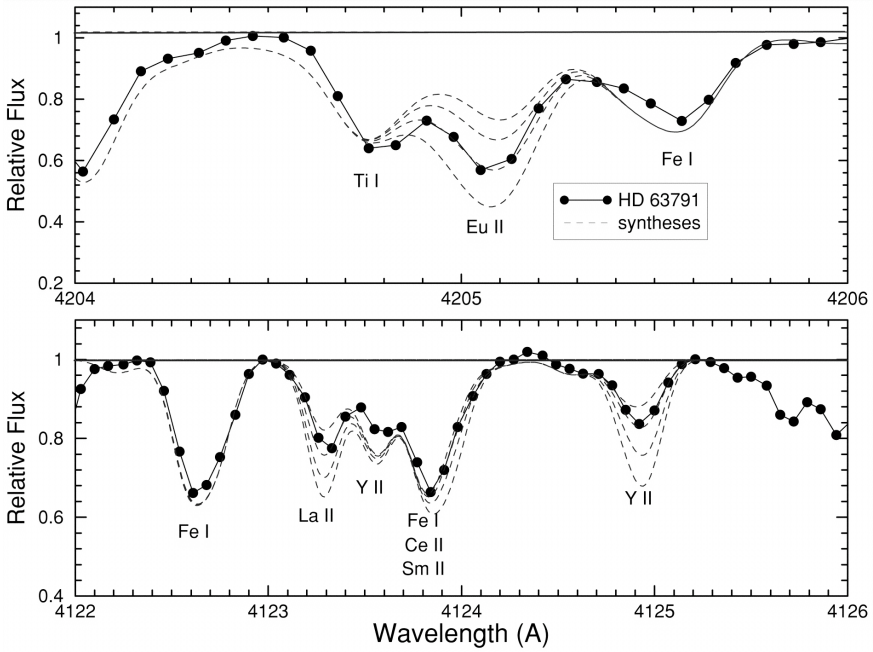

Figure 6.11: Example of spectral synthesis from which element abundances are deduced. The observed spectrum is represented by filled circles, while the lines show model spectra. All the model spectra have the same effective temperature, $T_{\rm eff} = 4725\,{\rm K}$, the same surface gravity, $\log g = 1.70$, and the same value of microturbulence, $\xi = 1.60\,{\rm km\ s^{-1}}$, but differ in the values of the abundances of the elements of interest, in this case the neutron-capture elements Eu, La, and Y. The solid line is deemed to fit best. The spectrum used for this abundance analysis has resolving power $R \equiv \lambda/\Delta\lambda \simeq 20\,000$ and signal-to-noise ratio ${\rm S/N} \simeq 100$; such high values are typical of the quality of spectra required for stellar abundance studies. (Figure reproduced from Burris et al. 2000, ApJ, 544, 302).

parameters, one is left with only one free parameter: the abundance of the element under consideration. By comparing the observed spectrum with model spectra computed for a range of values of, for example, Fe/H, the abundance of iron in the stellar photosphere can be deduced. (see Figure 6.11 for an example). Abundances so derived are usually referred to the solar abundance scale, since it is a prerequisite of the models that they reproduce the solar spectrum.

In the Milky Way, stellar metallicities vary from at most twice solar to $\sim 10^{-5.5}$ of solar; Figure 6.12 provides a vivid example of the weakening of stellar absorption lines with decreasing metallicity.

The solar metallicity scale is not without its problems! Some elements have proved difficult to measure accurately, and their abundances have undergone revisions, sometimes by non-negligible factors, in the last 10-20 years. Most people today adopt the Asplund et al. (2009) abundance scale reproduced in Figure 6.13. Note that, for historical reasons, element abundances are normally quoted by number (rather than by mass) on a log scale where H has value 12 (don't blame the messenger or, in this case, your lecturer!).

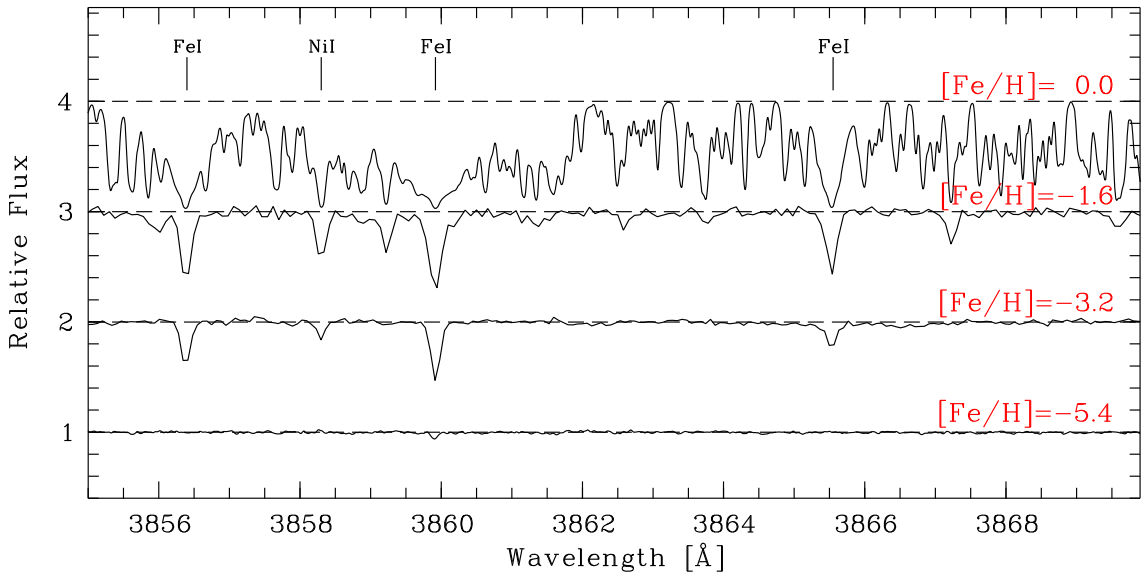

Figure 6.12: Spectral comparison of stars in the main-sequence turn-off region with different metallicities. Several absorption lines are marked. The variations in line strength reflect the different metallicities. From top to bottom: Sun with [Fe/H] = 0.0; G66-30 with [Fe/H] = −1.6; G64-12 with [Fe/H] = −3.2; and HE 1327−2326 with [Fe/H] = −5.4. (Figure reproduced from Frebel, A. 2010, Astronomische Nachrichten, 331, 474).

As an example, in the photosphere of the star HE 1327−2326 [Fe/H] = −5.4 (Figure 6.12). Recalling our definition: $[\mathrm{Fe/H}] \equiv \log(\mathrm{Fe/H})_{\mathrm{star}} - \log(\mathrm{Fe/H})_{\odot}$, we have $\log(\mathrm{Fe/H})_{\mathrm{star}} = 7.50 - 12 - 5.4 = -9.9$. In other words, in the photosphere of this very metal-poor star there is only 1 atom of Fe for every 10 billion atoms of H!

Table 1: Element abundances in the present-day solar photosphere. Also given are the corresponding values for CI carbonaceous chondrites (Lodders, Palme & Gail 2009). Indirect photospheric estimates have been used for the noble gases (Sect. 3.9).

	Elem.	Photosphere	Meteorites		Elem.	Photosphere	Meteorites
1	H	12.00	8.22 ± 0.04	44	Ru	1.75 ± 0.08	1.76 ± 0.03
2	He	$[10.93 \pm 0.01]$	1.29	45	Rh	0.91 ± 0.10	1.06 ± 0.04
3	Li	1.05 ± 0.10	3.26 ± 0.05	46	Pd	1.57 ± 0.10	1.65 ± 0.02
4	Be	1.38 ± 0.09	1.30 ± 0.03	47	Ag	0.94 ± 0.10	1.20 ± 0.02
5	B	2.70 ± 0.20	2.79 ± 0.04	48	Cd		1.71 ± 0.03
6	C	8.43 ± 0.05	7.39 ± 0.04	49	In	0.80 ± 0.20	0.76 ± 0.03
7	N	7.83 ± 0.05	6.26 ± 0.06	50	Sn	2.04 ± 0.10	2.07 ± 0.06
8	O	8.69 ± 0.05	8.40 ± 0.04	51	Sb		1.01 ± 0.06
9	F	4.56 ± 0.30	4.42 ± 0.06	52	Te		2.18 ± 0.03
10	Ne	$[7.93 \pm 0.10]$	-1.12	53	I		1.55 ± 0.08
11	Na	6.24 ± 0.04	6.27 ± 0.02	54	Xe	$[2.24 \pm 0.06]$	-1.95
12	Mg	7.60 ± 0.04	7.53 ± 0.01	55	Cs		1.08 ± 0.02
13	Al	6.45 ± 0.03	6.43 ± 0.01	56	Ba	2.18 ± 0.09	2.18 ± 0.03
14	Si	7.51 ± 0.03	7.51 ± 0.01	57	La	1.10 ± 0.04	1.17 ± 0.02
15	P	5.41 ± 0.03	5.43 ± 0.04	58	Ce	1.58 ± 0.04	1.58 ± 0.02
16	S	7.12 ± 0.03	7.15 ± 0.02	59	Pr	0.72 ± 0.04	0.76 ± 0.03
17	Cl	5.50 ± 0.30	5.23 ± 0.06	60	Nd	1.42 ± 0.04	1.45 ± 0.02
18	Ar	$[6.40 \pm 0.13]$	-0.50	62	Sm	0.96 ± 0.04	0.94 ± 0.02
19	K	5.03 ± 0.09	5.08 ± 0.02	63	Eu	0.52 ± 0.04	0.51 ± 0.02
20	Ca	6.34 ± 0.04	6.29 ± 0.02	64	Gd	1.07 ± 0.04	1.05 ± 0.02
21	Sc	3.15 ± 0.04	3.05 ± 0.02	65	Tb	0.30 ± 0.10	0.32 ± 0.03
22	Ti	4.95 ± 0.05	4.91 ± 0.03	66	Dy	1.10 ± 0.04	1.13 ± 0.02
23	V	3.93 ± 0.08	3.96 ± 0.02	67	Ho	0.48 ± 0.11	0.47 ± 0.03
24	Cr	5.64 ± 0.04	5.64 ± 0.01	68	Er	0.92 ± 0.05	0.92 ± 0.02
25	Mn	5.43 ± 0.05	5.48 ± 0.01	69	Tm	0.10 ± 0.04	0.12 ± 0.03
26	Fe	7.50 ± 0.04	7.45 ± 0.01	70	Yb	0.84 ± 0.11	0.92 ± 0.02
27	Co	4.99 ± 0.07	4.87 ± 0.01	71	Lu	0.10 ± 0.09	0.09 ± 0.02
28	Ni	6.22 ± 0.04	6.20 ± 0.01	72	Hf	0.85 ± 0.04	0.71 ± 0.02
29	Cu	4.19 ± 0.04	4.25 ± 0.04	73	Ta		-0.12 ± 0.04
30	Zn	4.56 ± 0.05	4.63 ± 0.04	74	W	0.85 ± 0.12	0.65 ± 0.04
31	Ga	3.04 ± 0.09	3.08 ± 0.02	75	Re		0.26 ± 0.04
32	Ge	3.65 ± 0.10	3.58 ± 0.04	76	Os	1.40 ± 0.08	1.35 ± 0.03
33	As		2.30 ± 0.04	77	Ir	1.38 ± 0.07	1.32 ± 0.02
34	Se		3.34 ± 0.03	78	Pt		1.62 ± 0.03
35	Br		2.54 ± 0.06	79	Au	0.92 ± 0.10	0.80 ± 0.04
36	Kr	$[3.25 \pm 0.06]$	-2.27	80	Hg		1.17 ± 0.08
37	Rb	2.52 ± 0.10	2.36 ± 0.03	81	Tl	0.90 ± 0.20	0.77 ± 0.03
38	Sr	2.87 ± 0.07	2.88 ± 0.03	82	Pb	1.75 ± 0.10	2.04 ± 0.03
39	Y	2.21 ± 0.05	2.17 ± 0.04	83	Bi		0.65 ± 0.04
40	Zr	2.58 ± 0.04	2.53 ± 0.04	90	Th	0.02 ± 0.10	0.06 ± 0.03
41	Nb	1.46 ± 0.04	1.41 ± 0.04	92	U		-0.54 ± 0.03
42	Mo	1.88 ± 0.08	1.94 ± 0.04				

Figure 6.13: The most recent compilation of solar element abundances by Asplund, Grevesse, Sauval, & Scott, P. 2009, ARAA, 47, 481.